

RESEARCH LETTER

10.1002/2017GL075547

Special Section:

The Arctic: An AGU Joint Special Collection

Key Points:

- A novel approach to estimate spring melt pond fraction from winter Sentinel-1 backscatter is developed
- The correlation between backscatter and melt pond fraction is strong at $r = -0.85$
- Large-scale maps of predicted spring melt pond fraction months in advance are possible

Supporting Information:

- Supporting Information S1
- Data Set S1
- Data Set S2
- Data Set S3

Correspondence to:

R. K. Scharien,
randy@uvic.ca

Citation:

Scharien, R. K., Segal, R., Nasonova, S., Nandan, V., Howell, S. E. L., & Haas, C. (2017). Winter Sentinel-1 backscatter as a predictor of spring Arctic sea ice melt pond fraction. *Geophysical Research Letters*, 44. <https://doi.org/10.1002/2017GL075547>

Received 5 SEP 2017

Accepted 19 NOV 2017

Accepted article online 27 NOV 2017

©2017. The Authors.

This is an open access article under the terms of the Creative Commons Attribution-NonCommercial-NoDerivs License, which permits use and distribution in any medium, provided the original work is properly cited, the use is non-commercial and no modifications or adaptations are made.

Winter Sentinel-1 Backscatter as a Predictor of Spring Arctic Sea Ice Melt Pond Fraction

Randall K. Scharien¹ , Rebecca Segal¹ , Sasha Nasonova¹, Vishnu Nandan², Stephen E. L. Howell³ , and Christian Haas⁴ 

¹Department of Geography, University of Victoria, Victoria, British Columbia, Canada, ²Cryosphere Climate Research Group, Department of Geography, University of Calgary, Calgary, Alberta, Canada, ³Climate Research Division, Environment and Climate Change Canada, Toronto, Ontario, Canada, ⁴Alfred Wegener Institute for Polar and Marine Research, Bremerhaven, Germany

Abstract Spring melt pond fraction (f_p) has been shown to influence September sea ice extent and, with a growing need to improve melt pond physics in climate and forecast models, observations at large spatial scales are needed. We present a novel technique for estimating f_p on sea ice at high spatial resolution from the Sentinel-1 satellite during the winter period leading up to spring melt. A strong correlation ($r = -0.85$) is found between winter radar backscatter and f_p from first-year and multiyear sea ice data collected in the Canadian Arctic Archipelago (CAA) in 2015. Observations made in the CAA in 2016 are used to validate a f_p retrieval algorithm, and a f_p prediction for the CAA in 2017 is made. The method is effective using the horizontal transmit and receive polarization channel only and shows promise for providing seasonal, pan-Arctic, f_p maps for improved understanding of melt pond distributions and forecast model skill.

Plain Language Summary Recent and well-documented changes in Arctic sea ice have introduced the need for timely and accurate seasonal forecasts of ice conditions. Seasonal forecasts of ice conditions will reduce the risks to humans and help preserve the fragile Arctic ecosystem by preventing accidents and spills. Recent studies have shown a link between the amount of surface meltwater flooding that occurs on sea ice in the spring, termed melt pond fraction, and the extent of sea ice that remains at the end of summer. This link is due to the ability of surface meltwater to absorb more sunlight compared to bare ice and snow. This study provides a new way to estimate the amount of surface meltwater flooding expected to occur on the sea ice in spring, using satellite data collected during the winter period. The results presented here provide a key link between winter and late summer sea ice conditions that will enhance the ability of forecasters to make accurate seasonal predictions several months in advance of the active summer period.

1. Introduction

The new Arctic sea ice regime is characterized by large declines summer ice extent in recent decades that have resulted in a shift from predominantly thicker multiyear sea ice (MYI) to thinner, seasonally decaying, first-year sea ice (FYI) (Maslanik et al., 2011; Meier et al., 2014; Stroeve et al., 2014). As sea ice acts as a barrier between the atmosphere and ocean, less (or thinner) ice is linked to increased radiative forcing, longer melt seasons, atmosphere and ocean effects, ecosystem changes, and threats to livelihoods of indigenous communities (Laxon et al., 2003; Markus et al., 2009; Perovich, Light, et al., 2007; Perovich & Polashenski, 2012; Pistone et al., 2014). Uncertainties regarding impacts of these changes in the Arctic under future warming scenarios, as well as increased economic interest in the region and commensurate risks to humans and the fragile Arctic ecosystem, have motivated efforts to improve sea ice predictions on seasonal to decadal time-scales (Eicken, 2013; Stroeve & Notz, 2015).

A critical component of the annual sea ice cycle and key feature required for skillful predictions of ice conditions is the formation of surface melt ponds in spring. Melt ponds form on the impermeable sea ice surface, reducing the areal albedo and enhancing heat uptake and melting rates (Fetterer & Untersteiner, 1998; Langleben, 1969; Maykut & Perovich, 1987). Melt ponds also allow light to penetrate the sea ice by 2–3 times, stimulating under ice productivity and further promoting melt (Arrigo et al., 2012; Inoue et al., 2008; Light et al., 2008; Morassutti & LeDrew, 1996). The physics of melt pond formation and evolution are well studied at the in situ scale (Eicken et al., 2002; Polashenski et al., 2012) but poorly understood at larger scales due to limitations on their detectability. For example, optical remote sensing techniques are limited by cloud cover

(Rösel et al., 2012; Tschudi et al., 2008). A link between the spring melt pond fractional coverage, or pond fraction (f_p), and the September minimum sea ice extent has been recently demonstrated (Schröder et al., 2014), prompting the need for better understanding of seasonal and spatial variations in f_p and the inclusion of melt pond physics in climate and forecast models. Consideration of f_p as a potential source of initialized predictions that, like sea ice thickness (Day et al., 2014), may lead to longer lead times in accurate seasonal predictions must be given. Regional f_p estimates will also help assess the underestimation of sea ice concentration from passive microwave data.

Sentinel-1 (S1) is an ongoing constellation mission with two satellites, S1A (2014 to present) and S1B (2016 to present), sharing the same near-polar orbital plane with a 180° orbital phasing difference. S1 provides virtually complete coverage of the Arctic sea ice every 6 days from C-band synthetic aperture radar (SAR) (Torres et al., 2012). Here we develop a novel approach using S1 backscatter and image texture measurements acquired during late winter conditions to provide a representative seasonal estimate of f_p expected within a few weeks after melt onset, since several feedback processes associated with melt will be initialized by conditions in this early period. Our approach, which isolates internally coherent, and externally discrete, zones of sea ice, is used to compare backscatter/texture and f_p and to create simple models for estimating f_p in advance of melting conditions. We apply the method over the entire Canadian Arctic Archipelago (CAA), which is a difficult region for climate models to resolve, providing f_p prediction maps for 2016 and 2017, and then discuss limitations of the approach.

2. Data and Methods

2.1. Data Description and Image Processing

Data used for development of f_p prediction models were collected from north of the Victoria Strait portion of the Northwest Passage, approximately 250 km northeast of the community of Cambridge Bay, Nunavut, in 2015 (Figure 1). Data for validating the f_p prediction models were collected in the south portion of Victoria Strait in 2016 (Figure 1). The area normally contains a mixture of thermodynamically grown FYI, deformed FYI, and MYI that are landfast from winter through the melt stages that lead up to the ice breakup and open water seasons (Haas & Howell, 2015).

Two consecutive S1 Extra Wide swath mode (EW) SAR scenes from the same orbit track were acquired on 5 April 2015, during cold, dry snow and ice conditions (Figure 1). The EW mode was designed for maritime use, particularly for imaging sea ice, with a 400 km wide swath and 20 m by 40 m range by azimuth resolutions (Torres et al., 2012). EW scenes comprise five subswaths spanning an incidence angle range of 19° to 47°. Scenes used here were acquired in dual-polarization horizontal transmit and receive polarization + horizontal transmit and vertical receive polarization (HH + HV) format and had been processed to Level-1 ground range detected format prior to delivery. Two cloud-free satellite GeoEye-1 (GE) visible-near-infrared image products of FYI-dominant and MYI-dominant sea ice zones of 72 km² and 118 km² size were collected on 25 June 2015, during the melt season. Each GE image product contained four channels between 450 and 920 nm at 1.7 m ground sample distance and a panchromatic channel at 0.41 m GSD. GE scenes were centered on an airborne winter survey track. On 19 April 2015, an airborne laser and electromagnetic (AEM) ice thickness survey was conducted to characterize late winter ice conditions during the period of maximum thickness and to support the ice type classifications carried out here (Haas & Howell, 2015; Haas et al., 2009). The profile was 718 km long and included surveys of Peel Sound, M'Clintock Channel, Victoria Strait, and Queen Maude Gulf. Measurements were spaced approximately 6 m apart, and two 20 km long sections that spatially coincided with the GE scenes were used (Figure 1).

In addition to the 2015 data used for the f_p prediction model development, collocated S1 and GE images in the Victoria Strait region were acquired in 2016 for validation of the algorithm. A S1 HH + HV scene was acquired on 9 April 2016, also during cold, dry snow and ice conditions, and a 100 km² cloud-free GE scene was acquired on 21 June 2016, during the melt season (Figure 1).

S1 images were processed by first removing thermal noise using noise estimate values provided in image annotation data sets. Bands HH and HV were calibrated to *gamma nought* backscatter, γ_{HH}^0 and γ_{HV}^0 , using the European Space Agency Sentinel-1 Toolbox v1.1.1. *Gamma nought* was used instead of the more common *sigma nought* since it is less sensitive to the undesirable influence of radar incidence angle on

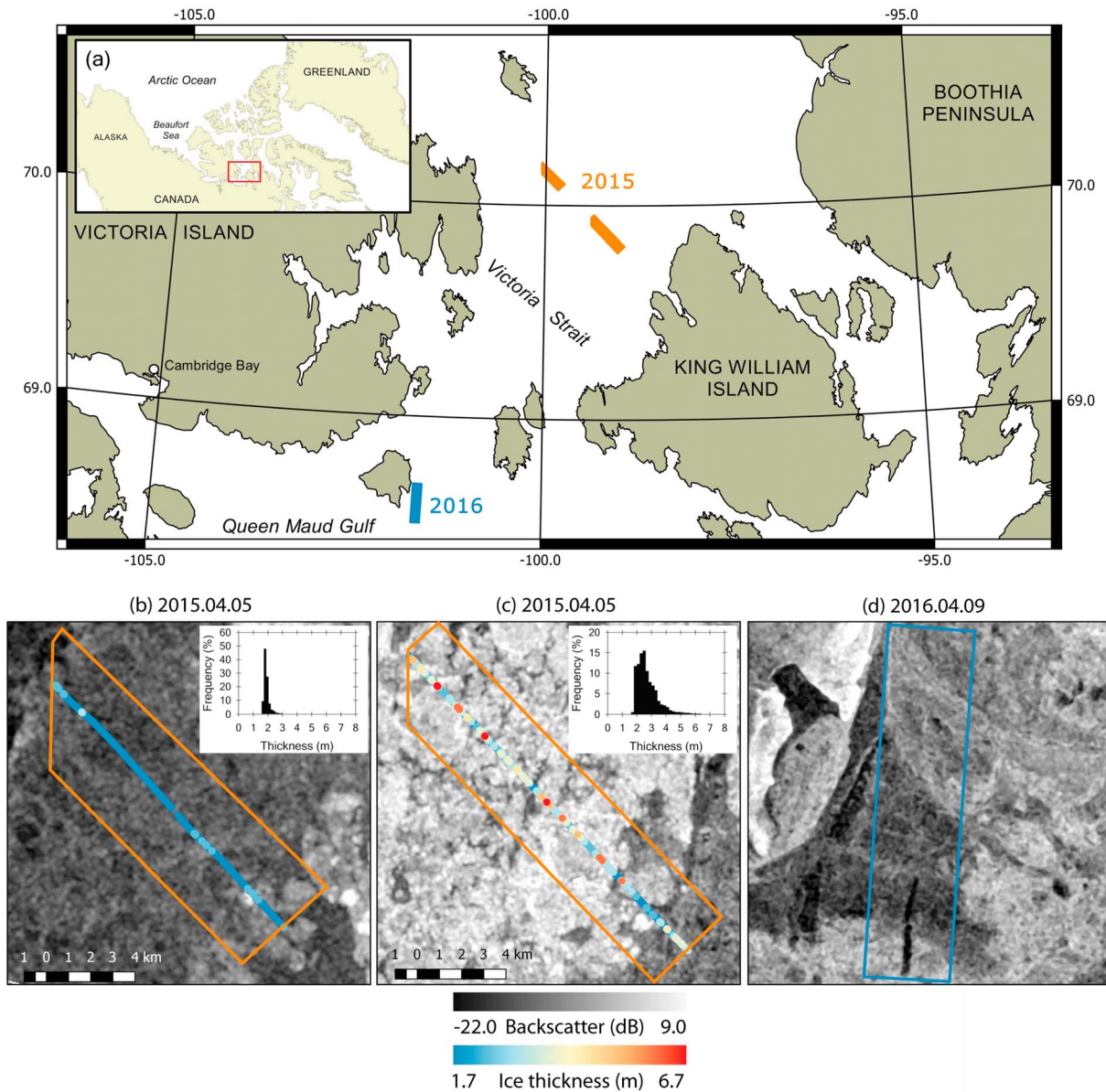


Figure 1. (a) Study area map including extents of GeoEye-1 optical satellite image acquisitions of melt pond covered sea ice in Victoria Strait in June 2015 and 2016. Extents of GeoEye-1 scenes collected in 2015 over predominantly smooth (b) first-year ice and (c) multiyear ice are shown in orange. (d) Extent of the GeoEye-1 scene collected in 2016 over smooth and deformed first-year ice is shown in blue. The backgrounds of Figures 1b–1d display the corresponding Sentinel-1 HH-channel backscatter images. Ice thickness data collected in 2015 are also shown in Figures 1a and 1b. The GeoEye-1 extents constrained the areas by which Sentinel-1 backscatter from cold, dry conditions was compared to spring melt pond fraction during model development (2015) and validation (2016) phases.

brightness levels (Small, 2011). This incidence angle effect was still apparent at near- and far-range extremes in γ^0 calibrated scenes, so data imaged at incidence angles below 26° and above 42° were eliminated. Calibrated γ_{HH}^0 and γ_{HV}^0 bands were speckle filtered using the Lee Filter and a 5 by 5 sliding window. Second-order image texture parameters contrast (CON), entropy (ENT), and correlation (COR) were derived from γ_{HH}^0 and γ_{HV}^0 bands using the gray-level co-occurrence matrix (GLCM) method developed by Haralick et al. (1973). These texture parameters were chosen since they cover the three major GLCM-based texture descriptor groups for quantifying spatial variations in gray levels (contrast, orderliness, and GLCM descriptive statistics) and are gray-level shift invariant (Clausi, 2002) (Text S1 in the supporting information). Additional sets of log-transformed backscatter and texture parameters were created by decibel (dB) and common logarithm (\log_{10}) transformations, respectively.

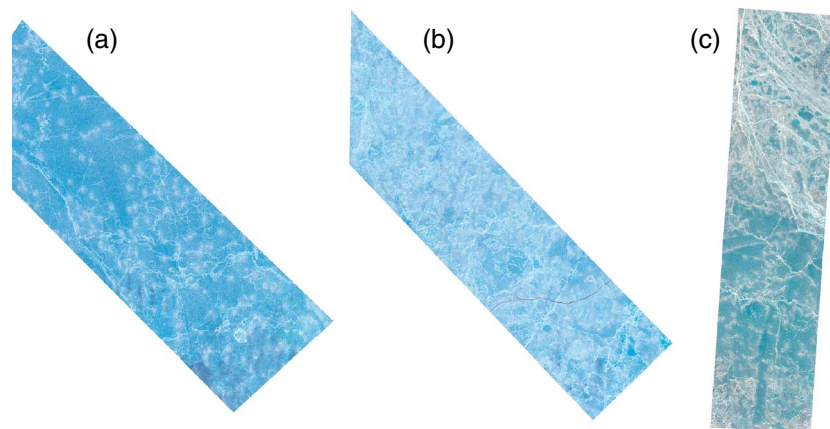


Figure 2. True-color representation of GeoEye-1 scenes of melt pond covered sea ice in the Canadian Arctic Archipelago, on (a) predominantly smooth first-year sea ice in 2015, (b) predominantly multiyear sea ice in 2015, and (c) a mixture of smooth and deformed first-year sea ice in 2016.

GE scenes were pan sharpened using the Gram-Schmidt algorithm, which fused the visible-near-infrared bands from each scene with their panchromatic image pair to produce a single-color image with a 0.5 m cell size (Figure 2). A supervised maximum likelihood approach was used to partition each scene into a binary classified image composed of snow/ice (0) and melt pond (1). The GE scenes from 2015 have overall classification accuracies of 98%. The GE scene from 2016 has an overall accuracy of 83% due largely to misclassified areas where melt ponds had drained, leaving a variegated and optically blue to blue-white ice surface representing a transition between pond and drained ice (Figure S1).

2.2. Estimating Melt Pond Fraction From S1 EW SAR

We used image objects (i.e., segments) to compare spatially coincident zones if S1 measured winter backscatter and GE estimated f_p from data collected in 2015 and to create f_p prediction models. First, the study areas, defined by the GE image extents, were segmented into discrete image objects using a bottom-up, region-merging, technique applied to the HH bands of S1 scenes (Benz et al., 2004). Several iterations of the segmentation algorithm were executed until the following criteria were met: (i) segments represented pans or floes of sea ice most likely to have unique dynamic and thermodynamic histories in agreement with the AEM thickness observations and (ii) in a spatial context, segments were internally coherent and externally heterogeneous such that they are unique in terms of roughness, backscatter, and most likely represent sea ice zones with unique spring melt pond formation mechanisms (Eicken et al., 2004; Polashenski et al., 2012). As sea ice floes are not always distinctly bounded, a hierarchical approach was used to address the indeterminacy of between-object boundaries. Three levels of segmentation were created by varying the spatial scale of segments; the intermediate scale is used here (Figure S2). Segments were labeled as FYI or MYI. Clear differences of thicker and more deformed MYI floes are also visible in the respective thickness histograms (Figure 1). Segments were used to calculate winter γ_{HH}^0 or γ_{HV}^0 and texture, and spring f_p , statistics and to estimate correlations using the *Pearson's product-moment correlation coefficient* (r). Optimized linear regression models for predicting f_p from backscatter and texture were derived using the stepwise, backward elimination, method (Text S2).

3. Results and Discussion

3.1. Relationship Between Backscatter and Melt Pond Fraction

Backscatter parameters γ_{HH}^0 (dB) and γ_{HV}^0 (dB) are significantly negatively correlated with f_p at $r = -0.85$ and $r = -0.86$, respectively (Figures 3a and 3b). Texture parameters CON and ENT from both γ_{HH}^0 and γ_{HV}^0 channels are also significantly negatively correlated with f_p and log scaling CON increases the strength of correlation with f_p in either case, γ_{HH}^0 and γ_{HV}^0 (Table S1). Regression model outputs and three linear regression equations for predicting f_p are given in Table S2. Regression model r^2 are all >0.7 and significant at $\alpha = 0.01$ (p value = 0.000). Models 1 and 2 use the HH polarization channel only; 2 is a negligible improvement over 1

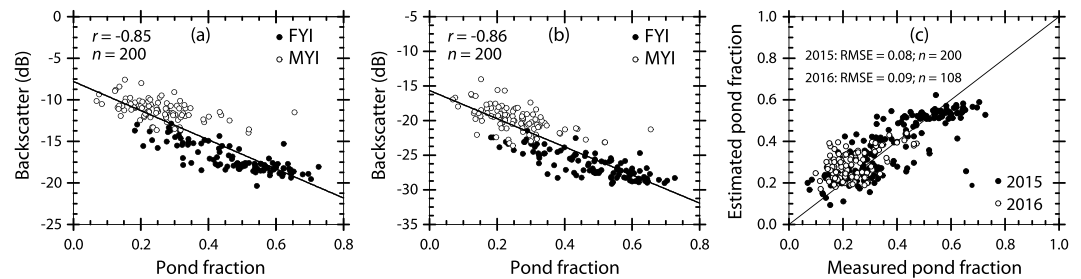


Figure 3. Correlations (a) between winter γ_{HH}^0 and spring f_p and (b) between winter γ_{HV}^0 and spring f_p . Each sample in Figures 3a and 3b was derived from a spatially coincident image segment of winter Sentinel-1 image backscatter and spring GeoEye-1 f_p , labeled first-year ice (FYI) or multiyear ice (MYI). (c) Predicted against measured f_p for the 2015 data set operating in hindcast mode and for the 2016 validation data set. Each marker in Figure 3c represents an individual image segment composed of estimated f_p , from a Sentinel-1 image using model 2, compared to measured f_p , from a classified GeoEye-1 image.

by way of inclusion of the texture parameter ENT. ENT is a measure of disorder, such that its inclusion is intuitive given that areas of smooth FYI are relatively uniform in terms of gray-level (tone) variations in SAR images compared to areas including deformation and MYI features (Soh & Tsatsoulis, 1999). Model 3 uses the HV polarization channel which, for S1, has a much smaller signal-to-noise ratio compared to HH and is differentially influenced by system noise across the subswaths that make up the EW product (Nagler et al., 2015). These system constraints are likely to limit the application of models requiring the HV channel of S1.

Figure 3c shows the predicted and observed f_p obtained by applying model 2 (Table S2) to the validation data set collected in 2016, as well as to the 2015 data set in a hindcast mode. Model 2 in hindcast mode performs as expected from Table S2; the RMSE is 0.08, and there is negligible bias. The RMSE of the validation data set is 0.09, and a positive bias of 0.05 is apparent as overestimation of f_p in areas ranging from approximately 0.10 to 0.35. This bias is likely due to the difference in sea ice conditions in 2016. The validation data set comprises several ridges, whereas the original data set comprises discrete FYI and MYI floes. During winter, ridged ice and MYI both have bright and overlapping signatures in SAR imagery. It is possible that the spring f_p on MYI floes is higher than it is for ridged FYI since the lateral distribution of surface meltwater is even more limited by ridged features than it is by the weathered hummocks and old melt ponds on MYI. Overall, the data in Figure 3c indicate a tendency for the model to underestimate f_p in areas roughly 0.6 and above. This underestimation points to possible lower limit in the sensitivity of γ_{HH}^0 to variations in the winter ice surface features that determine f_p on smooth FYI. The influence of snow thickness on f_p variations for smooth FYI areas with similar topographical and C-band backscattering characteristics is not captured by the model.

3.2. Spatial Distribution of Melt Pond Fraction

Sea ice f_p mapping during the later winter period provides a critical link between the winter ice cover and conditions during spring/summer periods. Several energy and mass exchange process occurring at the atmosphere-ice-ocean interface are enhanced by the presence of melt ponds, with rates tied closely to the magnitude of f_p . Predictions of f_p provide a measure of the preconditioning of the sea ice cover for energy uptake, light transmittance, upper ocean productivity, and gas and contaminant uptake driven by air-pond interaction mechanisms during spring. Furthermore, the ability to make accurate seasonal forecasts of the September minimum sea ice extent should be improved by f_p predictions in the winter leading up to spring.

Predictions of f_p in the CAA in 2016 and 2017, derived from S1 EW mode images collected during cold, dry snow and ice conditions and by applying model 1 (Table S2), are shown along with corresponding ice charts produced by the Canadian Ice Service (Figure 4). Small portions of the 2016 map, which required data collected when only S1A was operational and coverage more limited, were filled using data outside the incidence angle limit of our algorithm (26° to 42°). This inclusion resulted in a striping effect related to swath seams, apparent north of Banks and Victoria Islands in the western portion of the CAA. In 2017 S1A and S1B were both operational, so that the incidence angle criterion was met and no striping occurred. The high spatial resolution of S1 reveals complex patterns in f_p associated with variable distributions of ice types within the CAA, as well as year-to-year variations at local to regional scales. The overall f_p for the CAA decreased from

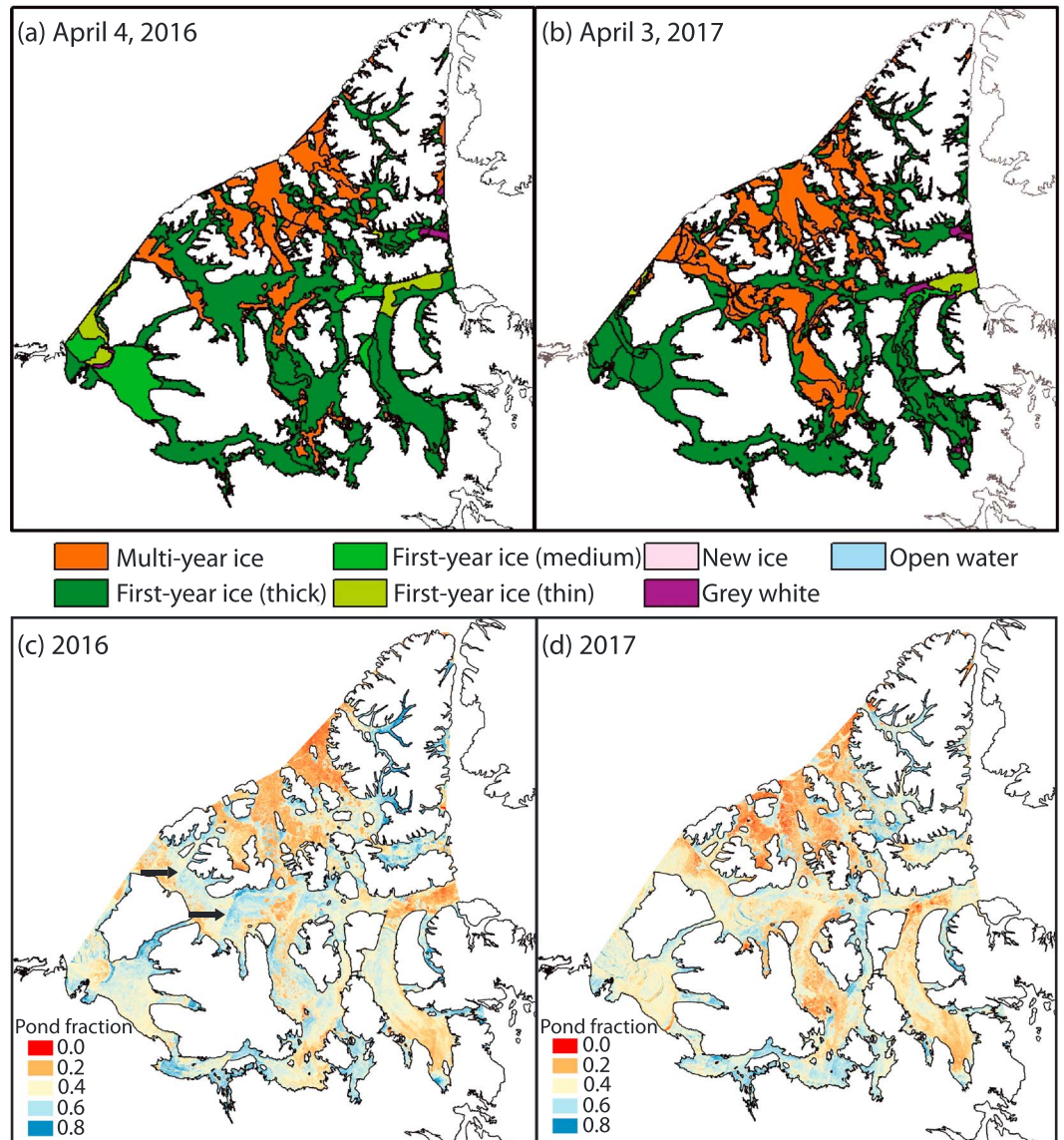


Figure 4. Canadian ice service produced ice charts for the Canadian Arctic Archipelago in (a) 2016 and (b) 2017. Predicted f_p for the Canadian Arctic Archipelago in (c) 2016 and (d) 2017, derived from Sentinel-1 images acquired during cold, dry snow and ice conditions (February to April). Black arrows in the 2016 map indicate locations where the striping effect caused by portions of swaths falling outside the required Sentinel-1 incidence angle range is apparent.

0.43 in 2016 to 0.40 in 2017 (Figure 5a). The apparent decrease in predicted f_p is likely from the presence of more MYI in the region in 2017, notably in portions of the Northwest Passage sea route compared to 2016 (Figure 4b). A 3% overall decrease in f_p can lead to a profound change in the energy deposited in the ice-ocean system (Perovich, Nghiem, et al., 2007). Moreover, Figure 5b shows areas within the CAA where f_p varies by as much as 40% between 2016 and 2017, indicating that much different f_p -driven atmosphere-ice-ocean exchanges were occurring in these areas from year to year.

One caveat concerning this approach is that it does not account for temporal dynamics in f_p . It is well known that f_p is not static; rather, it evolves as a function of competing melt rate-driven meltwater inputs, surface topography-driven hydraulic gradients driving meltwater flow, and drainage processes related to the permeability of the ice (Eicken et al., 2002). The f_p evolves differently over time on FYI than it does on MYI. The f_p is generally higher on FYI throughout the ponding season, as meltwater is less topographically constrained and ponds spread rapidly over larger areas (Grenfell & Perovich, 2004). This is captured by the model presented

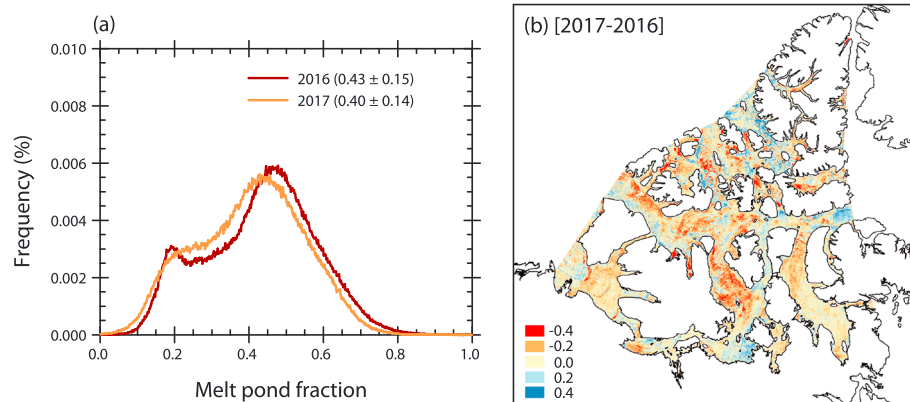


Figure 5. (a) Predicted melt pond fraction distributions for the Canadian Arctic Archipelago in 2016 and 2017 and (b) a difference map indicating a large amount of spatial variability.

here. However, measurements of f_p made on undeformed FYI at Barrow, Alaska, and Resolute Bay, Nunavut, have shown that competing meltwater inputs and outflows on thinner FYI lead to variations in f_p by 20 to 50% after the initial formation stage (Eicken et al., 2004; Landy et al., 2014; Polashenski et al., 2012). Furthermore, melt ponds can completely drain from FYI prior to complete decay or disintegration as hydraulic connectivity with the ocean is achieved while the hydraulic head is positive. Melt pond water is more likely to be retained on MYI throughout the ponding season and fluctuations in f_p are less dramatic than for FYI.

Examination of ancillary optical remote sensing data sets illustrated that melt ponds formed 12–14 days prior to the collection of GE scenes in 2015 used to create the f_p prediction model (not shown). In the acquired GE scenes, we observed f_p on FYI to be consistently high and up to 0.73, with no visual evidence of pond drainage. Accordingly, our algorithm applies to the stage of the seasonal melt pond cycle that falls close to the seasonal peak in f_p , where flooding is determined by rapid surface snowmelt combined with meltwater retention by relatively cold, impermeable ice, and contrasts in f_p between FYI and MYI are mainly due to topography (Eicken et al., 2002). This is an important period for determining the fate of the ice, as the initial phase of f_p plays a pivotal role in determining local variations in rates of heat uptake, ice microstructure evolution and vertical water transport, and further stages of pond evolution.

4. Conclusions

A novel approach for estimating the spring melt pond fraction on sea ice during the late preceding winter period is presented in this study. The approach uses backscatter information collected by the Sentinel-1 mission, a two-satellite constellation of near-polar-orbiting SARs that provide regular and complete coverage of the Arctic region at high spatial resolution (40 m pixel spacing). The results of this study demonstrate that the spring sea ice melt pond fraction can be predicted on a seasonal basis using a forecast method based on the correlation between winter radar backscatter and spring pond fraction. The simplest model, using calibrated backscatter from the HH polarization channel only, demonstrated an RMSE of 0.09. This is reasonable considering that it is in proximity to error bounds of direct estimates of spring melt pond fraction using optical and radar data (Istomina et al., 2015; Rösel et al., 2012; Scharien et al., 2014). Using data aggregated according to sea ice segments representing unique zones of sea ice, deriving the relationship between winter backscatter and spring melt pond fraction was made possible. Predictions of melt pond fraction can be made during the thermodynamically stable winter period, well in advance of melting conditions and several months prior to the annual minimum extent. These predictions will lead to enhancements in seasonal forecasts of sea ice conditions by providing a critical link between the winter sea ice cover and its thermodynamic condition during spring melt. We observed a lower f_p in the landfast ice of the CAA in 2017 compared to 2016, which suggests that this region is more resistant to melt in 2017 and may contribute to a higher summer minimum sea ice extent compared to 2016. Regional forecasts of pond fraction for pack ice will have to consider the influence of ice dynamics.

Sentinel-1 operates in C-band frequency, making it part of a long series of SARs providing sea ice information used in operational ice charting and mapping studies. Owing to its legacy in sea ice applications, data continuity including the constellation format is expected beyond the timeline of Sentinel-1, beginning with the launch of Canada's RADARSAT Constellation Mission in 2018. Further work will enable a complete assessment of model skill and model refinement by inclusion of more sea ice regimes, particularly the sea ice pack outside of the Canadian Arctic Archipelago. Implementation of these predictions into seasonal sea ice forecasts and outlooks is forthcoming.

Acknowledgments

Data collection and analysis were supported by funds from Natural Sciences and Engineering Research Council (NSERC) Discovery Grant (DG), Marine Environmental Observation, Prediction, and Response Network (MEOPAR), and the Changing Earth Science Network, part of the European Space Agency's Support To Science Element (STSE). The authors declare no financial conflicts of interests. Sentinel-1 data are available from the online database Copernicus Open Access Hub (<https://scihub.copernicus.eu/>). GeoEye-1 data are available at a cost from the DigitalGlobe database (<https://browse.digitalglobe.com/>). Supporting data are included as Data Set S1. Under certain terms and conditions, GeoEye-1 data may be available free of charge from the European Space Agency.

References

- Arrigo, K. R., Perovich, D. K., Pickart, R. S., Brown, Z. W., van Dijken, G. L., Lowry, K. E., ... Swift, J. H. (2012). Massive phytoplankton blooms under Arctic sea ice. *Science*, 336(6087), 1408. <https://doi.org/10.1126/science.12150651408>
- Benz, U. C., Hofmann, P., Willhauck, G., Lingenfelder, I., & Heynen, M. (2004). Multi-resolution, object-oriented fuzzy analysis of remote sensing data for GIS-ready information. *ISPRS Journal of Photogrammetry and Remote Sensing*, 58(3–4), 239–258. <https://doi.org/10.1016/j.isprsjprs.2003.10.002>
- Clausi, D. A. (2002). An analysis of co-occurrence texture statistics as a function of grey level quantization. *Canadian Journal of Remote Sensing*, 28(1), 45–62. <https://doi.org/10.5589/m02-004>
- Day, J. J., Hawkins, E., & Tietsche, S. (2014). Will Arctic sea ice thickness initialization improve seasonal forecast skill? *Geophysical Research Letters*, 41, 7566–7575. <https://doi.org/10.1002/2014GL061694>
- Eicken, H. (2013). Ocean science: Arctic sea ice needs better forecasts. *Nature*, 497(7450), 431–433. <https://doi.org/10.1038/497431a>
- Eicken, H., Grenfell, T. C., Perovich, D. K., Richter-Menge, J. A., & Frey, K. (2004). Hydraulic controls on summer Arctic pack ice albedo. *Journal of Geophysical Research*, 109, C08007. <https://doi.org/10.1029/2003JC001989>
- Eicken, H., Krouse, H. R., Kadko, D., & Perovich, D. K. (2002). Tracer studies of pathways and rates of meltwater transport through Arctic summer sea ice. *Journal of Geophysical Research*, 107(C10), 8046. <https://doi.org/10.1029/2000JC000583>
- Fetterer, F., & Untersteiner, N. (1998). Observations of melt ponds on Arctic sea ice. *Journal of Geophysical Research*, 103(C11), 24,821–24,835. <https://doi.org/10.1029/98JC02034>
- Grenfell, T. C., & Perovich, D. K. (2004). Seasonal and spatial evolution of albedo in a snow-ice-land-ocean environment. *Journal of Geophysical Research*, 109, C01001. <https://doi.org/10.1029/2003JC001866>
- Haas, C., & Howell, S. E. L. (2015). Ice thickness in the Northwest Passage. *Geophysical Research Letters*, 42, 7673–7680. <https://doi.org/10.1002/2015GL065704>
- Haas, C., Lobach, J., Hendricks, S., Rabenstein, L., & Pfaffling, A. (2009). Helicopter-borne measurements of sea ice thickness, using a small and lightweight, digital EM system. *Journal of Applied Geophysics*, 67(3), 234–241. <https://doi.org/10.1016/j.jappgeo.2008.05.005>
- Haralick, R. M., Shanmugan, K., & Dinstein, I. (1973). Textural features for image classification. *IEEE Transactions on Systems, Man, and Cybernetics*, 3(6), 610–621.
- Inoue, J., Kikuchi, T., & Perovich, D. K. (2008). Effect of heat transmission through melt ponds and ice on melting during summer in the Arctic Ocean. *Journal of Geophysical Research*, 113, C05020. <https://doi.org/10.1029/2007JC004182>
- Istomina, L., Heygster, G., Huntemann, M., Schwarz, P., Birnbaum, G., Scharien, R., ... Katsev, I. (2015). Melt pond fraction and spectral sea ice albedo retrieval from MERIS data—Part 1: Validation against in situ, aerial, and ship cruise data. *The Cryosphere*, 9(4), 1551–1566. <https://doi.org/10.5194/tc-9-1551-2015>
- Landy, J., Ehn, J., Shields, M., & Barber, D. (2014). Surface and melt pond evolution on landfast first-year sea ice in the Canadian Arctic Archipelago. *Journal of Geophysical Research: Oceans*, 119, 3054–3075. <https://doi.org/10.1002/2013JC009617>
- Langleben, M. P. (1969). Albedo and degree of puddling of a melting cover of sea ice. *Journal of Glaciology*, 8(54), 407–412. <https://doi.org/10.1017/S002214300002699X>
- Laxon, S., Peacock, N., & Smith, D. (2003). High interannual variability of sea ice thickness in the Arctic region. *Nature*, 425(6961), 947–950. <https://doi.org/10.1038/nature02050>
- Light, B., Grenfell, T. C., & Perovich, D. K. (2008). Transmission and absorption of solar radiation by arctic sea ice during the melt season. *Journal of Geophysical Research*, 113, C03023. <https://doi.org/10.1029/2006JC003977>
- Markus, T., Stroeve, J. C., & Miller, J. (2009). Recent changes in Arctic sea ice melt onset, freezeup, and melt season length. *Journal of Geophysical Research*, 114, C12024. <https://doi.org/10.1029/2009JC005436>
- Maslanik, J., Stroeve, J., Fowler, C., & Emery, W. (2011). Distribution and trends in Arctic sea ice age through spring 2011. *Geophysical Research Letters*, 38, L13502. <https://doi.org/10.1029/2011GL047735>
- Maykut, G., & Perovich, D. (1987). The role of shortwave radiation in the summer decay of a sea ice cover. *Journal of Geophysical Research*, 92(C7), 7032–7044. <https://doi.org/10.1029/JC092iC07p07032>
- Meier, W. N., Hovelsrud, G. K., van Oort, B. E. H., Key, J. R., Kovacs, K. M., Michel, C., ... Reist, J. D. (2014). Arctic sea ice in transformation: A review of recent observed changes and impacts on biology and human activity. *Reviews of Geophysics*, 52, 185–217. <https://doi.org/10.1002/2013RG000431>
- Morassutti, M. P., & LeDrew, E. F. (1996). Albedo and depth of melt ponds on sea ice. *International Journal of Climatology*, 16(7), 817–838. [https://doi.org/10.1002/\(SICI\)1097-0088\(199607\)16:7%3C817::AID-JOC44%3E3.0.CO;2-5](https://doi.org/10.1002/(SICI)1097-0088(199607)16:7%3C817::AID-JOC44%3E3.0.CO;2-5)
- Nagler, T., Rott, H., Hetzenecker, M., White, J., & Potin, P. (2015). The Sentinel-1 mission: New opportunities for ice sheet observations. *Remote Sensing*, 7(7), 9371–9389. <https://doi.org/10.3390/rs70709371>
- Perovich, D. K., Light, B., Eicken, H., Jones, K. F., Runciman, K., & Nghiem, S. V. (2007). Increasing solar heating of the Arctic Ocean and adjacent seas, 1979–2005: Attribution and role in the ice-albedo feedback. *Geophysical Research Letters*, 34, L19505. <https://doi.org/10.1029/2007GL031480>
- Perovich, D. K., Nghiem, S. V., Markus, T., & Schweiger, A. (2007). Seasonal evolution and interannual variability of the local solar energy absorbed by the Arctic sea ice–ocean system. *Journal of Geophysical Research*, 112, C03005. <https://doi.org/10.1029/2006JC003558>
- Perovich, D. K., & Polashenski, C. (2012). Albedo evolution of seasonal Arctic sea ice. *Geophysical Research Letters*, 39, L08501. <https://doi.org/10.1029/2012GL051432>
- Pistone, K., Eisenman, I., & Ramanathan, V. (2014). Observational determination of albedo decrease caused by vanishing Arctic sea ice. *Proceedings of the National Academy of Sciences of the United States of America*, 111(9), 3322–3326. <https://doi.org/10.1073/pnas.1318201111>

- Polashenski, C., Perovich, D., & Courville, Z. (2012). The mechanisms of sea ice melt pond formation and evolution. *Journal of Geophysical Research*, 117, C01001. <https://doi.org/10.1029/2011JC007231>
- Rösel, A., Kaleschke, L., & Birnbaum, G. (2012). Melt ponds on Arctic sea ice determined from MODIS satellite data using an artificial neural network. *The Cryosphere*, 6(2), 431–446. <https://doi.org/10.5194/tc-6-431-2012>
- Scharien, R. K., Hochheim, K., Landy, J., & Barber, D. G. (2014). First-year sea ice melt pond fraction estimation from dual-polarisation C-band SAR—Part 2: Scaling in situ to Radarsat-2. *The Cryosphere*, 8(6), 2163–2176. <https://doi.org/10.5194/tc-8-2163-2014>
- Schröder, D., Feltham, D. L., Flocco, D., & Tsamados, M. (2014). September Arctic sea-ice minimum predicted by spring melt-pond fraction. *Nature Climate Change*, 4(5), 353–357. <https://doi.org/10.1038/nclimate2203>
- Small, D. (2011). Flattening gamma: Radiometric terrain correction for SAR imagery. *IEEE Transactions on Geoscience and Remote Sensing*, 49(8), 3081–3093. <https://doi.org/10.1109/TGRS.2011.2120616>
- Soh, L.-K., & Tsatsoulis, C. (1999). Texture analysis of SAR sea ice imagery using gray level co-occurrence matrices. *IEEE Transactions on Geoscience and Remote Sensing*, 37(2), 780–795. <https://doi.org/10.1109/36.752194>
- Stroeve, J. C., Markus, T., Boisvert, L., Miller, J., & Barrett, A. (2014). Changes in Arctic melt season and implications for sea ice loss. *Geophysical Research Letters*, 41, 1216–1225. <https://doi.org/10.1002/2013GL058951>
- Stroeve, J., & Notz, D. (2015). Insights on past and future sea-ice evolution from combining observations and models. *Global and Planetary Change*, 135, 119–132. <https://doi.org/10.1016/j.gloplacha.2015.10.011>
- Torres, R., Snoeij, P., Geudtner, D., Bibby, D., Davidson, M., Attema, E., ... Rostan, F. (2012). GMES Sentinel-1 mission. *Remote Sensing of Environment*, 120, 9–24. <https://doi.org/10.1016/j.rse.2011.05.028>
- Tschudi, M. A., Maslanik, J. A., & Perovich, D. K. (2008). Derivation of melt pond coverage on Arctic sea ice using MODIS observations. *Remote Sensing of Environment*, 112, 2605–2614. <https://doi.org/10.1016/j.rse.2007.12.009>